Check for updates

Bayesian optimization of nanophotonic electromagnetic shielding with very high visible transparency

MINGXUAN LI,[1] MICHAEL J. MCCOURT,[2] ANTHONY J. GALANTE,[1] AND PAUL W. LEU[1,3,4,*]

[1] *Department of Industrial Engineering, University of Pittsburgh, Pittsburgh, PA 15261, USA*
[2] *SigOpt, an Intel company, San Francisco, CA 94104, USA*
[3] *Department of Mechanical Engineering, University of Pittsburgh, Pittsburgh, PA 15261, USA*
[4] *Department of Chemical Engineering, University of Pittsburgh, Pittsburgh, PA 15261, USA*
*pleu@pitt.edu

Abstract: Transparent electromagnetic interference (EMI) shielding is needed in many opto-electronic applications to protect electronic devices from surrounding radiation while allowing for high visible light transmission. However, very high transmission (over 92.5%), high EMI shielding efficiency (over 30 dB) structures have yet to be achieved in the literature. Bayesian optimization is used to optimize different nanophotonic structures for high EMI shielding efficiency (SE) and high visible light transmission ($\bar{T}_{vis}$). Below 90% average visible light transmission, sandwich structures consisting of high index dielectric/silver/high index dielectric films are determined to be optimal, where they are able to achieve 43.1 dB SE and 90.0% $\bar{T}_{vis}$. The high index of refraction dielectric layers reduce absorption losses in the silver and can be engineered to provide for antireflection through destructive interference. However, for optimal EMI shielding with $\bar{T}_{vis}$ above 90%, the reflection losses at the air/dielectric interfaces need to be further reduced. Optimized double sided nanocone sandwich structures are determined to be best where they can achieve 41.2 dB SE and 90.8% $\bar{T}_{vis}$ as well as 35.6 dB SE and 95.1% $\bar{T}_{vis}$. K-means clustering is utilized to show the performance of characteristic near-Pareto optimal structures. Double sided nanocone structures are shown to exhibit omnidirectional visible transmission with $SE = 35.6$ dB and over 85% $\bar{T}_{vis}$ at incidence angles of 70°.

1. Introduction

As electronic devices and systems have become increasingly utilized and complex, there is a growing need to develop new types of electromagnetic interference (EMI) shielding [1]. EMI shielding is required to reduce coupling of electronic components to surrounding radiation, which could reduce the functionality or accuracy of electronic devices or shorten their lifetimes [2]. EMI shielding is also needed to better protect humans from health hazards associated with long-term exposure to electromagnetic waves [3]. Metal films, boxes, or meshes have been traditionally used as EMI shielding [1]. However, these metal structures tend to be heavy and thick [4], and their cost of manufacturing is high [5]. New lightweight EMI shielding technologies are needed that may provide for high shielding efficiency (SE).

EMI shielding that is additionally transparent is also needed for many optoelectronic applications, which require visible light to pass through with high efficiency. Applications such as windows, displays, mobile devices, and wearables all have a need for both high visible transparency and strong shielding. There has been a lot of work done with metal micromeshes or microgrids due to their ability to achieve both high transparency and low sheet resistance [6–8]. Nickel meshes fabricated by photolithography and transfer printed onto ITO have achieved 40 dB SE and 92% transmission [9]. Multi-ring aluminum meshes fabricated by photolithography

and dry etching have exhibited 27 dB SE and 90% transmission [10]. Graphene integrated with metal microgrids has also been demonstrated for EMI shielding due to their high performance as transparent conductors [11]. A graphene/nickel mesh film was demonstrated with 12.1 dB SE and 83% transmission [12]. And a metal-mesh hybrid graphene film exhibited an average SE of 25.5 dB and 91% transmission [13].

Another type of transparent EMI shielding material are metal thin films [14,15]. Silver (Ag) is the most widely used material for this application due to its high conductivity. To improve the visible transmission of the Ag film, different high index dielectric materials have been explored to surround the Ag. ITO/Ag-Cu/ITO was demonstrated to have 96.5% transmission and 26 dB SE [16]. Yuan *et al.* reported that ZnO/Ag/ZnO sandwich structures could achieve 35 dB SE and 88.9% transmission in the visible range [17]. Additional sandwich structures could be included to improve performance at the cost of additional fabrication complexity [17].

One challenge in transparent EMI shielding has been creating structures with high SE over 30 dB and very high average visible transmission over 92.5%. Nickel micromeshes on ITO have exhibited 40 dB but only have 92% average visible transmission [9]. On the other hand, EMI shielding materials with high average visible transmission over 92.5% have had low SE. ITO/Ag-Cu/ITO sandwich structure have exhibited 96.5% average visible transmission but only 26 dB SE [16]. Multi layer salt water has 94.2% average visible transmission but only 20 dB SE [18]. New visible EMI shielding structures are needed that may simultaneously achieve high SE over 30 dB and very high average visible transmission over 92.5%.

In this work, a variety of nanophotonic structures were simulated and optimized by a Bayesian strategy. In particular nanocones with high refractive indices were integrated with sandwich structures. Metal thin film, dielectric/metal/dielectric sandwich, top nanocone (TNC), bottom nanocone (BNC), and double sided nanocone (DNC) structures were all simulated and optimized. For average visible transparency under 90%, sandwich structures were determined to be optimal. Sandwich structures are able to achieve 41.6 SE and 90.0% average visible transparency with 10 nm Ag. The surrounding high index dielectric layers reduce absorption by reducing the electric field in the Ag. Reflection losses are also reduced due to destructive interference. However, like other structures in the literature, sandwich structures demonstrate a substantial drop in SE for visible transmission above 92.5%. DNC structures demonstrate the best performance for visible transmission over 90%, where the nanocones are needed to reduce reflection between the high-index dielectric and the air by grading the index of refraction. DNCs demonstrate 41.2 dB SE with 90.8% average visible transmittance as well 35.6 dB SE with 95.1% average visible transmittance. K-means clustering is performed on near-Pareto optimal sandwich and DNC structures to illustrate their characteristic performances and structural parameters. DNC structures exhibit omnidirectional transmission. With 42.4 dB SE (10 nm Ag), the average visible transmission is 90.1% at normal incidence, 83.8% at 60 degrees incidence and 71.2% at 70 degrees incidence. With 37.2 dB SE (5 nm Ag), the average visible transmission is 83.6% at normal incidence, 77.0% at 60 degrees incidence and 69.7% at 70 degrees incidence. This work demonstrates the potential of achieving both high EMI shielding efficiency (over 30 dB) and very high transmittance (over 92.5%) using DNC structures.

2. Simulation and optimization

2.1. Structure geometry and objective functions

Figure 1 shows the five different structures evaluated in this paper: (a)(i) Ag thin films (TFs), (ii) Ag thin films surrounded with a titanium dioxide (TiO_2) layer at the bottom and top (sandwiches), and three different nanocone (NCs) structures: (iii) top NC Ag thin films (TNCs), (iv) bottom NC Ag thin films (BNCs), and (v) Ag thin film sandwiches with double sided nanocones (DNCs). NC-type structures have been demonstrated as effective structures for antireflection [19] and can be fabricated by maskless reactive ion etching methods [20–23]. For TFs, the only structure

parameter is the thickness of the Ag layer. For sandwiches, the structure is defined by the thickness of the Ag layer as well as the thickness of each side of titanium dioxide. For TNCs sandwiches and BNCs, seven parameters were used to describe the structure, where the difference between the two structures is TNCs only have NCs on top and the BNCs only have NCs on the bottom side. DNCs have NCs on both sides and are defined by ten parameters as shown in Fig. 1(b): the thickness of the Ag (t_{Ag}), the thickness of the top and bottom titanium dioxide layers (t_{top}, t_{bot}), the top cone's top radius (r_{top}), bottom radius (r_{bot}), and height (h); and the bottom cone's top radius (r_{btop}), bottom radius (r_{bbot}), and height(h_b); and finally, the nanocone pitch (a). The NC structures are assumed to be in a square lattice. The design parameter space is set to $t_{Ag} \in [3, 20]$ nm, $t_{top} \in [5, 100]$ nm, $t_{bot} \in [5, 100]$ nm, $r_{top} \in [10, 200]$ nm, $r_{bot} \in [10, 200]$ nm, $h \in [50, 800]$ nm, $r_{btop} \in [10, 200]$ nm, $r_{bbot} \in [10, 200]$ nm, $h_b \in [50, 800]$ nm, $a \in [20, 400]$ nm, with the constraints $r_{top} \leq r_{bot}$ and $2r_{bot} \leq a$, $r_{btop} \geq r_{bbot}$ and $2r_{btop} \leq a$. All the parameters are discretized to integers, and the step size of cone height is set to 50 nm.
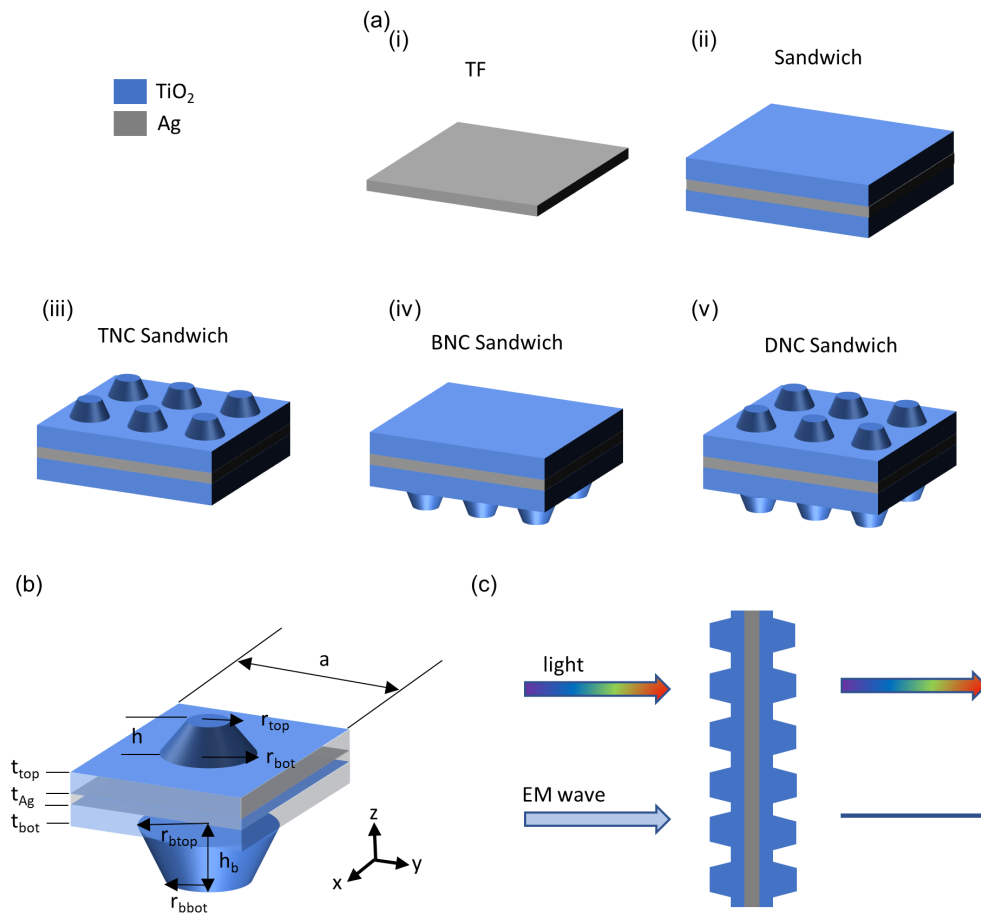

Fig. 1. Schematics of the five different structures studied: (a)(i) Ag thin film (TF), (ii) titanium dioxide sandwiched Ag thin film (sandwich), (iii) top nanocone Ag thin film (TNC); (iv) bottom nanocone Ag thin film (BNC); and (v) double sided nanocone sandwich Ag thin film (DNC). (b) Parameters used in optimizing the NC structures. (c) Schematic showing the two objective functions of maximizing visible transmittance and maximizing SE in radio frequencies.

The design problem consists of a multi-objective optimization problem where the two objective functions to be maximized are the shielding efficiency (SE) and the average visible transmission ($\bar{T}_{vis}$) (Fig. 1(c)). The SE is defined by

$$SE = 20 \log_{10} \left(1 + \frac{\eta_0}{2R_s} \right) \tag{1}$$

where $\eta_0 = 377\Omega$ is the impedance of free space and $R_s = \frac{\rho}{t_{Ag}}$ is the sheet resistance of the conductive thin film where $\rho = 1.59 \times 10^{-8}$ $\Omega \cdot$m is the bulk resistivity of silver. The SE is calculated based on the sheet resistance of the conductive thin film, which is valid when the impedance of the film is much lower than that of free space and the thickness of the film is smaller than the skin depth [16]. In this study, we focus on Ag thicknesses of only less than 20 nm, which is much less than the skin depth of Ag at the frequency range of $1 \sim 40$ GHz ($0.317 \sim 2$ μm).

The average visible transmission is obtained over the visible wavelength range of 400 to 700 nm:

$$\bar{T}_{vis} = \frac{\int_{400}^{700} T(\lambda) d\lambda}{\int_{400}^{700} d\lambda}. \tag{2}$$

Transmission simulations are performed using the finite difference time domain method. Periodic boundary conditions are used to create a square lattice and perfectly match layers (PML) were used at the top and bottom of the simulation supercell. For angle dependence simulations, the broadband fixed angle source technique (BFAST) is used [24]. The mesh setting is set differently in each structure region. For the thin film regions, $dx = 10$ nm, $dy = 10$ nm, and $dz = 1$ nm and for the NCs, $dx = a/10$, $dy = a/10$, and $dz = 50$ nm. The Ag index of refraction values were obtained from the CRC handbook [25], and the titanium dioxide values from Sarkar *et. al.* [26]

2.2. Multiobjective Bayesian optimization

To explore the 10-dimensional design space of DNCs and identify satisfactory designs, we employed a sample-efficient sequential decision making methodology. This multiobjective Bayesian optimization process iteratively models the relationship between the parameters and the two design metrics (SE and $\bar{T}_{vis}$), and then it suggests a next best configuration to evaluate to learn more about high-performing designs [19]. The results of that evaluation are then added to the model which powers the next suggested configuration. We use independent Gaussian processes to model the objectives [27]. These are assumed to have constant mean and anisotropic radial C^4 Matérn covariance kernels with length scales determined through maximum likelihood estimation. The acquisition function is a modified expected improvement function detailed in our earlier work [19]; at each iteration, the acquisition function is optimized using differential evolution [28], modified to function in the constrained domain defined.

The search that we conduct defines satisfactory outcomes as those structures with EMI shielding greater than 30 dB and average visible transmission greater than 80%. We guide our search by applying constraints to the multiobjective optimization process in the fashion described in our previous work [20]. Constraint active search is utilized to provide additional insight into near-Pareto optimal structures, which may be more useful for manufacturing purposes than focusing exclusively on Pareto optimal structures [29].

3. Result and discussion

The results of the simulations and optimization are shown in Fig. 2 for the five structures: (a)(i) TFs; (ii) Sandwiches; (iii) TNCs; (iv) BNCs and (v) DNCs. For the TF structure, the performance for all integer thicknesses between 3 and 20 nm were evaluated. For each of the sandwich,

TNC, BNC, and DNC structures, 500 designs were evaluated using Bayesian optimization. The Pareto frontier for each structure is shown with a line. Figure 2(b) shows a comparison of the Pareto frontier of the five different types of structures. The right y-axis in Fig. 2(b) shows the thickness of silver for each structure. Below 90% average visible transmission the best performing structures are the sandwich structures. These structures consist of Ag thin films over 10 nm thick. Sandwich structures are able to achieve 41.6 SE and 90.0% $\bar{T}_{vis}$ with 10 nm silver. However, sandwich structures have a substantial drop in SE performance in order to achieve $\bar{T}_{vis}$ above 90%. Sandwich structures are able to achieve 33.7 dB SE with 90.6 % $\bar{T}_{vis}$. For average visible transparency above 90%, the best performing structures are the DNCs. DNCs are able to achieve 41.6 dB SE and 90.8% $\bar{T}_{vis}$ with 10 nm Ag and 35.6 dB SE and 95.1% $\bar{T}_{vis}$ with 5 nm Ag. For Ag thin films above 10 nm thicknesses, the sandwich structures perform better than the DNC sandwich structures.
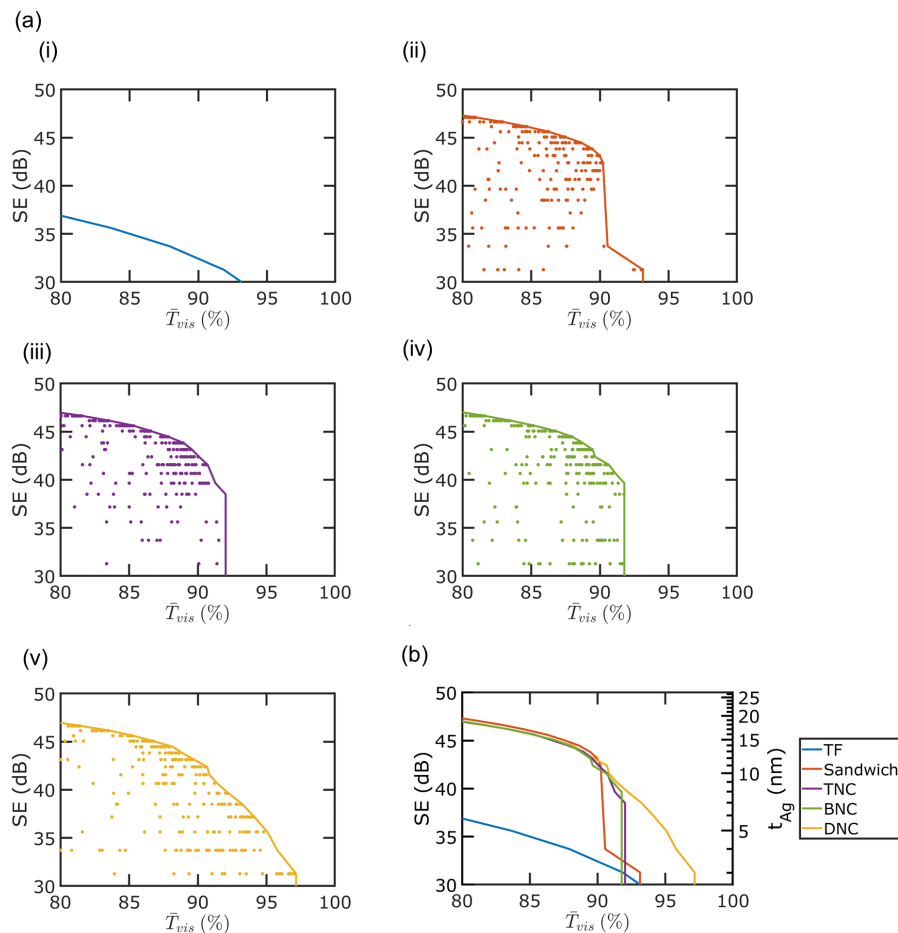

Fig. 2. SE and $\bar{T}_{vis}$ of (a)(i) TFs, (ii) Sandwiches, (iii) TNCs, (iv) BNCs, and (v) DNCs. The Pareto frontier is shown with a line. (b) Comparison of the Pareto frontier of all five structures.

The best performing structures for $\bar{T}_{vis} < 90\%$ are the sandwich structures. To explore the relationship between structural parameters in the sandwich structures, we use K-means clustering on near Pareto optimal structures to determine what types of sandwich structures enable high performance. Figure 3(a) shows the four clusters of sandwich structures with the brown cluster

achieving between 46.1 to 46.6 SE and 81.0 to 84.7% $\bar{T}_{vis}$, the cyan cluster achieving between 44.5 to 45.6 SE and 86.0 to 88.7% $\bar{T}_{vis}$, the blue cluster achieving between 42.4 to 44.5 SE and 88.0 to 90.2% $\bar{T}_{vis}$, and the yellow cluster achieving between 31.3 to 33.7 SE and 90.5 to 93.1% $\bar{T}_{vis}$. Figure 3(a)(ii) plots the normalized parameters of the four near Pareto-optimal clusters, where it can be seen that the structures in each cluster are similar. In Fig. 3(b), the characteristic shape of each cluster is plotted where the structure nearest the centroid of each cluster is shown. Table 1 shows the parameters of the characteristic structures. DNC structures are the best performing structures for $\bar{T}_{vis}$>90%.

Another data exploration is performed on near Pareto optimal DNC structures with $\bar{T}_{vis}$>90% (Fig. 4). In Fig. 4(a), the near-Pareto optimal structures are plot in different colors for different clusters. We use four clusters to show the trend of near-Pareto optimal structures. Two characteristic near-Pareto optimal structures are shown for each of the four clusters (Fig. 4(b)). Table 2 shows the performance and parameters for the characteristic shapes in each cluster. In the purple region, the top NCs are the smallest nanowire possible (r_{top} = r_{bot} = 10 nm), and the bottom NCs are nanowire-like (r_{btop} ≈ r_{bbot}). In the red region, the top NCs are also nanowires (r_{top} = r_{bot}). The top nanowire diameters are about half that of the pitches, and the bottom diameters of the bottom nanocone are about the same as the pitches. In the green region, the bottom diameters of the bottom NCs are close to the pitch, but the bottom diameters of the top NC are a little bit smaller than the pitch. In the black region, the bottom diameters of the top and bottom NCs are close to the pitches. The top NCs have the smallest top diameters possible, while the bottom NCs have slightly larger top diameters.
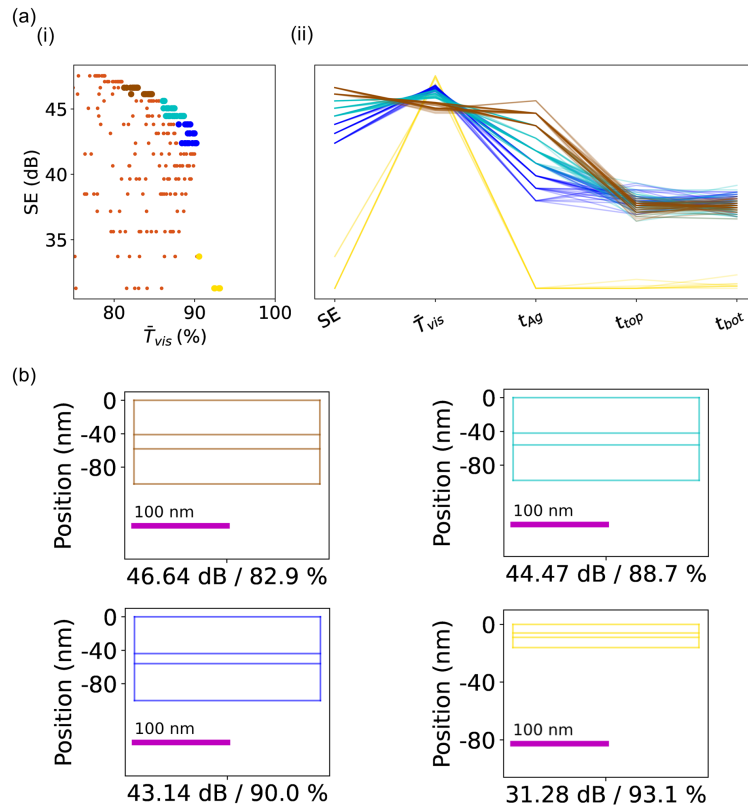

Fig. 3. (a)(i) Clusters of near-Pareto optimal sandwich structures and (ii) normalized parameter plot. (b) Characteristic shape of sandwich structures.
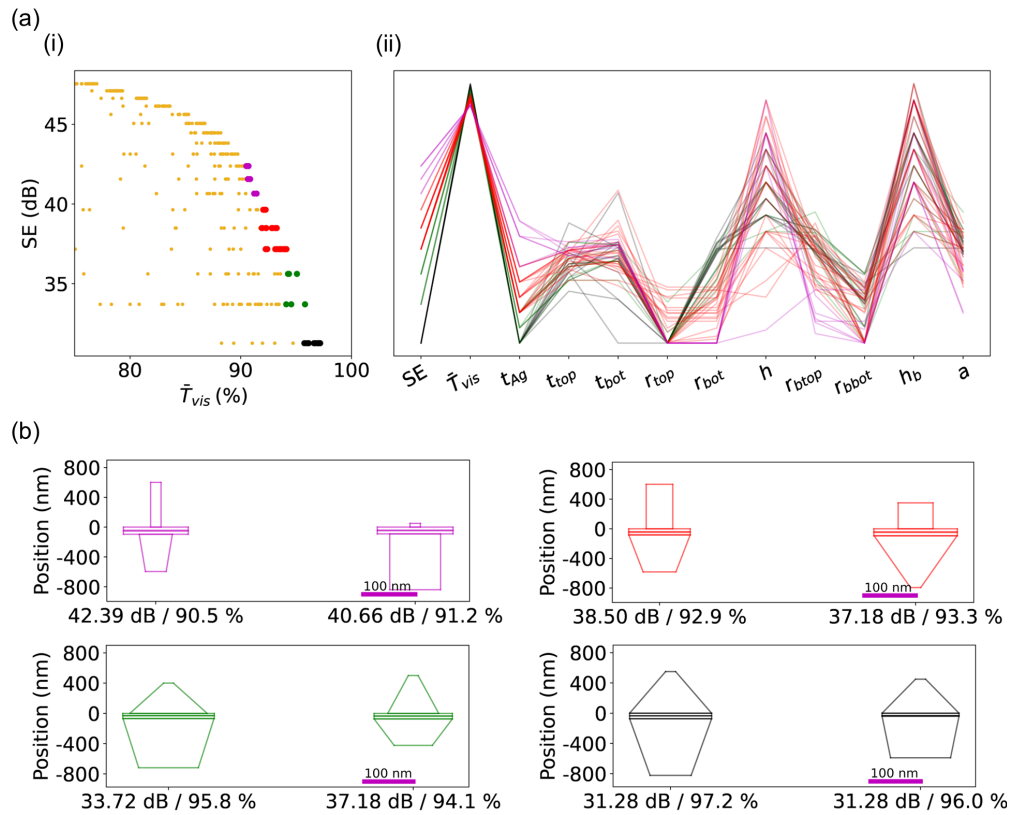
(a)

(i)

(ii)

(b)

Fig. 4. (a)(i) Simulation result clustering scatter plot and (ii) normalized parameter plot for DNC Sandwich. (b) Characteristic shape of DNC Sandwich structure.

Table 1. Sandwich performance and parameters for each cluster.

Cluster Color	SE (dB)	$\bar{T}_{vis}$ (%)	t_{Ag} (nm)	t_{top} (nm)	t_{bot} (nm)
Brown	46.6	82.9	17	41	42
Cyan	44.5	88.7	14	42	42
Blue	43.1	90.0	12	44	44
Yellow	31.3	93.1	3	6	7

The near Pareto-optimal structures in the purple cluster are more sandwich-like where the sub-wavelength nanowires function like a thin film with a constant effective index of refraction. In the red region, the near Pareto-optimal structures transition into structures that are more nanowire-like on top and NC-like on bottom. Finally, the highest transmission structures have NCs on both top and bottom and the highest performing structures have NCs that fill out the space.

Figure 5 plots the transmission (red), reflection (green), and absorption (blue) of (a) TFs, (b) sandwiches and (c) DNCs on the Pareto Frontier. The SE is shown on the left *y*-axis and the thickness of the silver is shown on the right *y*-axis. The transmission, reflection, and absorption sum up to 100% for each structure. The sandwich and DNC structures have lower absorption compared to the TFs. The use of high index dielectric layers surrounding the metal

Table 2. DNC performance and structural parameters for each cluster.

Cluster	SE	$\bar{T}_{vis}$	t_{Ag}	t_{top}	t_{bot}	r_{top}	r_{bot}	h	r_{btop}	r_{bbot}	h_b	a
Color	(dB)	(%)	(nm)	(nm)	(nm)	(nm)	(nm)	(nm)	(nm)	(nm)	(nm)	(nm)
Purple	42.4	90.5	10	42	43	10	10	600	32	20	500	125
	40.7	91.2	8	40	42	10	10	50	49	49	750	146
Red	38.5	92.9	7	39	36	26	26	600	60	32	500	120
	37.2	93.3	6	42	46	34	34	350	81	10	700	163
Green	33.7	95.8	4	28	36	10	79	400	93	61	650	187
	37.2	94.1	5	33	35	10	52	500	80	39	350	160
Black	31.3	97.2	3	33	37	10	82	550	82	41	750	164
	31.3	96.0	3	31	5	10	77	450	77	60	550	154

film reduces the optical electric field in Ag thin film and thus, reduces absorption loss in the Ag [30]. Additionally, the dielectric layers also reduce reflection losses in the visible spectrum by destructive interference [31]. However, for transmission above 90%, the reflection losses become more substantial part of the total optical losses. DNCs enable higher $\bar{T}_{vis}$ as the grading of the index of refraction enables lower reflection losses at the dielectric/air interfaces.
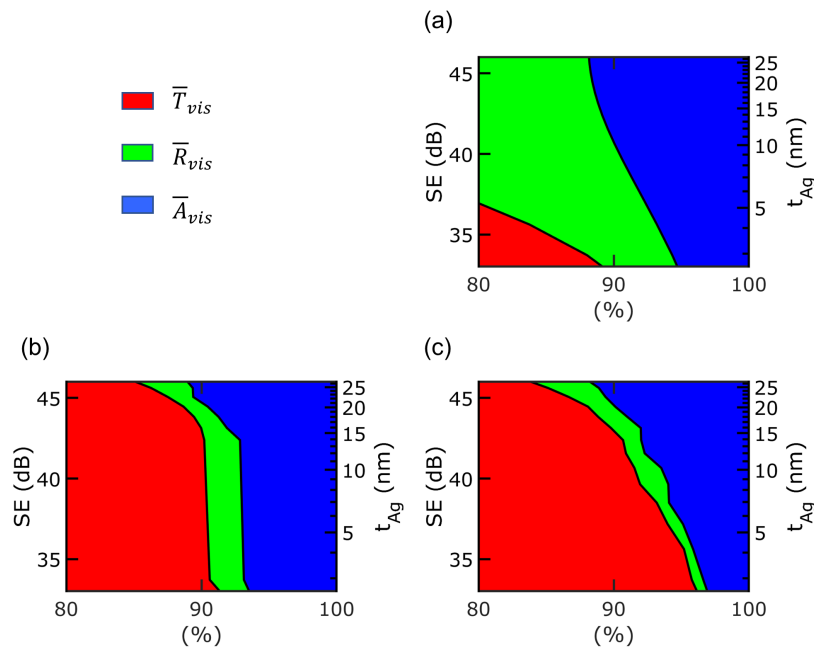

Fig. 5. Visible range light transmission, reflection, and attenuation ratio plot for (a) TFs, (b) Sandwiches, and (c) DNC Sandwiches.

To further examine how electromagnetic (EM) waves interact with through different structures, we simulated the electric field intensity of Pareto optimal structures with a 400 to 700 nm transverse electromagnetic (TEM) light source and plot the center cross section of each structure. Figure 6 shows color contour plots of the E-field intensity of optimized structures, where the white dashed lines are the boundary of the Ag film and the blacked dashed lines are the boundary of the titanium dioxide. Figure 6(a) shows the highest average visible transmission structures when $SE = 35.6$ dB and $t_{Ag} = 5$ nm. For TF structures (Fig. 6(a),(i)), the light reflects off the

front surface and is attenuated by the conductive Ag, and the average visible transmission is 83.6%. For the sandwich structure (Fig. 6(a),(ii)), the thickness of the top high index layer is 40 nm and the thickness of the bottom high index layer is 41 nm. The high index layer increases the transmission of the structure to 88.0% average visible transmission. The DNC structure (Fig. 6(a),(iii)) is able to achieve the highest average visible transmission of the three structures (95.1%) as the electric field concentrates in the spaces between the nanocones.
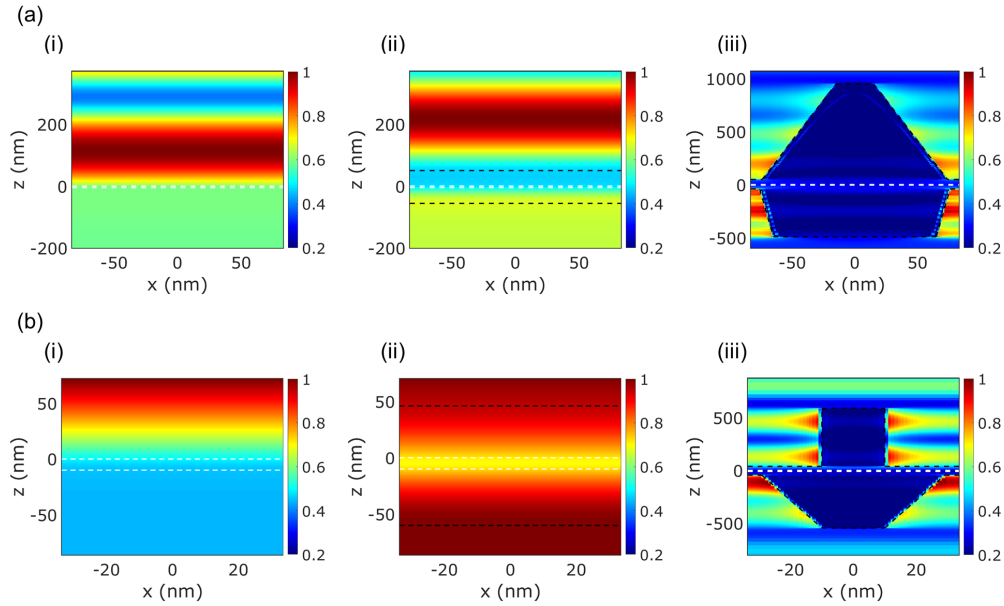

Fig. 6. Normalized electric field density distribution for (a) highest average visible transmission structures when t_{Ag} = 5 nm and SE = 35.6 dB: (i) TF (83.6% $\bar{T}_{vis}$); (ii) Sandwich (88.0% $\bar{T}_{vis}$); (iii) DNC Sandwich (95.1% $\bar{T}_{vis}$). (b) Highest average visible transmission structures when t_{Ag} = 10 nm and SE = 41.6 dB: (i) TF (61.6% $\bar{T}_{vis}$); (ii) Sandwich (90.0% $\bar{T}_{vis}$); (iii) DNC Sandwich (90.8% Transmission $\bar{T}_{vis}$).

Figure 6(b) shows the highest average visible transmission structures for when t_{Ag} = 10 nm and SE = 41.6 dB. For the (i) TF structure, the decay of the electric field intensity is large, and the average visible transmission is 61.6%. In the (ii) sandwich structure, the E-field intensity decreases between top high index layer and the metal layer, but due to constructive interference, the transmission is 89.8%. The intensity of light decreases in the silver layer and the average visible transmission is improved. The (iii) DNC sandwich structure doesn't perform better than the sandwich structure as most of the loss in the sandwich structures is due to absorption in the metal and reflection losses are very small.

High transmission over a wider range of angle is preferred in many light emitting or light extraction devices [19,31,32]. Figure 7 plots the average visible transmission as a function of incidence angle for the same six optimized structures shown in Fig. 6. Figure 7(a) shows the angle dependence for the three structures with SE = 35.6 dB (t_{Ag} = 5 nm) for (i) TE and TM-polarized light respectively and (ii) the average of TE- and TM-polarized light. The DNC sandwich structure has the highest visible transmission over a wide range of angles until 55 degrees for both light polarizations. Above 55 degrees, the thin film and sandwich structures have higher transmission for TM incident light. The average transmission of the DNC Sandwich out performs all the other structures over all angles. The DNC Sandwich has the best omnidirectional transmission performance. For the Ag TF, the average visible transmission is 83.6% at normal

incidence, 77.0% at 60 degrees incidence and 69.7% at 70 degrees incidence. For the sandwich structures, the average visible transmission is 89.3% at normal incidence, 85.2% at 60 degrees incidence and 78.6% at 70 degrees incidence. For the DNCs, the average visible transmission is 95.1% at normal incidence, 91.0% at 60 degrees incidence and 85.9% at 70 degrees incidence.
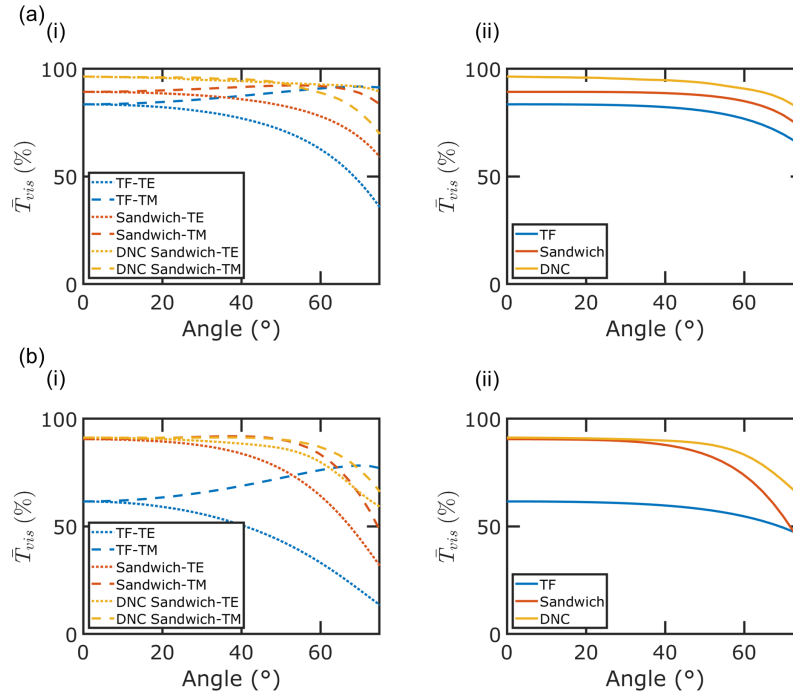

Fig. 7. Angular dependence of $\bar{T}_{vis}$ for optimized TFs, sandwiches, and DNCs. Angular dependence of optimized structures when (a) t_{Ag} = 5 nm and *SE* = 35.6 dB and (b) t_{Ag} = 10 nm and EMI SE = 41.6 dB. (i) Angular dependence of TE and TM incident visible light, and (ii) average of TE and TM incidence visible light.

Figure 7(b) shows the angle dependency when t_{Ag} = 10 nm for (i) TE- and TM-polarized light and (ii) the TE and TM average. The sandwich structure performs better in most regions than just the Ag TF. For the Ag TF, the average visible transmission is 61.6% at normal incidence, 54.9% at 60 degrees incidence and 49.5% at 70 degrees incidence. For the sandwich structure, the average visible transmission is 89.8% at normal incidence, 74.5% at 60 degrees incidence and 54.5% at 70 degrees incidence. For the DNC structure, the average visible transmission is 90.1% at normal incidence, 83.8% at 60 degrees incidence and 71.2% at 70 degrees incidence.

We compare the Pareto Frontier of our DNC structure to other published work (Fig. 8). As discussed above and can be seen in this plot, previous studies on EMI shielding have failed to demonstrate high SE above 30 dB with very high $\bar{T}_{vis}$ over 92.5%. Experimental results for graphene/Al mesh [36], Ag-Ni mesh [37], CuO-Cu mesh [38], multi-layer graphene [13], multi-ring array Al mesh [10], multi layer salt water [18] and ITO/Ag-Cu/ITO [16] are all shown. Simulation results for IZO/Ag/IZO [33], AZO/Ag/AZO [34], and ZnO/Ag/ZnO [17] are also shown, where these structures have similar performance to ours. Structures with $\bar{T}_{vis}$ over 92.5% have only achieved 26 dB SE with $\bar{T}_{vis}$ = 96.5% for ITO/Ag-Cu/ITO [16]. Multi layer salt water has demonstrated 20 dB SE with $\bar{T}_{vis}$ = 94.2% [18]. DNCs may outperform these structures and achieve 41.2 dB SE with 90.8% $\bar{T}_{vis}$ and 35.6 dB SE with 95.1% $\bar{T}_{vis}$.
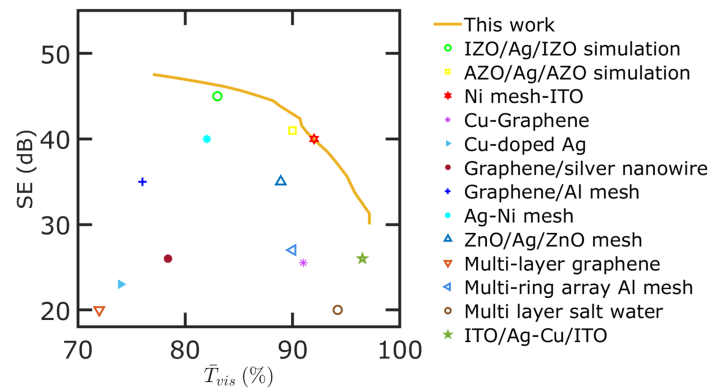
Fig. 8. Comparison of EMI SE (dB) and Transmission of NC Sandwich in this work to other simulation and experimental work in the literature: IZO/Ag/IZO simulation [33], AZO/Ag/AZO simulation [34], Ni mesh-ITO [9], Cu-graphene [13], Cu-doped Ag [16], Graphene/silver nanowire [35], Graphene/Al mesh [36], Ag-Ni mesh [37], ZnO/Ag/ZnO [17], multi-layer graphene [13], multi-ring array Al mesh [10], multi-layer salt water [18], and ITO/Ag-Cu/ITO [16].

4. Conclusion

In conclusion, we demonstrate a simulation and optimization strategy for the design of various nanophotonic transparent EMI shielding structures. Bayesian optimization is applied to five different nanophotonic structures: metal thin films, sandwich structures, top nanocone structures, bottom nanocone structures, and double-sided nanocone structures. It is determined that sandwich structures achieve the best performance for average visible transmission under 90%. Sandwich structures are able to achieve 41.6 EMI SE with 90.0% $\bar{T}_{vis}$. Single-sided nanocone structures offer some benefits over sandwich structures above 90% average visible transmission. However, the best performing structures for over 90% average visible transmission are double-sided nanocone structures. Double-sided nanocone structures are able to achieve 35.6 dB SE with 95.1% average visible transmission and 41.2 dB SE with 90.8% average visible transmission. These structures exhibit omnidirectional transmission with high transmission even at incidence angles over 70°. These structures provide for very high transmission due to optical impedance reduction and antireflection. These simulations demonstrate a pathway to high SE, very high visible transparency EMI shielding through nanophotonic structures.

Disclosures. The authors declare no conflicts of interest.

Data availability. The data that support the findings of this study are available from the corresponding author upon reasonable request.

References

1. S. Geetha, K. K. S. Kumar, C. R. K. Rao, M. Vijayan, and D. C. Trivedi, "EMI shielding: Methods and materials—A review," J. Appl. Polym. Sci. **112**, 2073–2086 (2009).
2. Y. Bhattacharjee and S. Bose, "Core–shell nanomaterials for microwave absorption and electromagnetic interference shielding: A review," ACS Appl. Nano Mater. **4**(2), 949–972 (2021).

3. F. Ozdemir and A. Kargi, "Electromagnetic waves and human health," in *Electromagnetic Waves*, V. Zhurbenko, ed. (IntechOpen, 2011), Chap. 22.

4. B. Wen, M. Cao, M. Lu, W. Cao, H. Shi, J. Liu, X. Wang, H. Jin, X. Fang, W. Wang, and J. Yuan, "Reduced graphene oxides: Light-weight and high-efficiency electromagnetic interference shielding at elevated temperatures," Adv. Mater. **26**, 3484–3489 (2014).

5. J. Liang, Y. Wang, Y. Huang, Y. Ma, Z. Liu, J. Cai, C. Zhang, H. Gao, and Y. Chen, "Electromagnetic interference shielding of graphene/epoxy composites," Carbon **47**(3), 922–925 (2009).

6. Z. Zhou, S. B. Walker, M. LeMieux, and P. W. Leu, "Polymer-Embedded Silver Microgrids by Particle-Free Reactive Inks for Flexible High-Performance Transparent Conducting Electrodes," ACS Appl. Electron. Mater. **3**(5), 2079–2086 (2021).

7. T. Gao, P.-S. Huang, J.-K. Lee, and P. W. Leu, "Hierarchical metal nanomesh/microgrid structures for ordered and uniform transparent electrodes," RSC Adv. **5**(87), 70713–70717 (2015).

8. T. Gao, S. Haghanifar, M. G. Lindsay, P. Lu, M. I. Kayes, B. D. Pafchek, Z. Zhou, P. R. Ohodnicki, and P. W. Leu, "Fundamental performance limits and haze evaluation of metal nanomesh transparent conductors," Adv. Opt. Mater. **6**, 1700829 (2018).

9. Z. ying Jiang, W. Huang, L. sen Chen, and Y. hua Liu, "Ultrathin, lightweight, and freestanding metallic mesh for transparent electromagnetic interference shielding," Opt. Express **27**(17), 24194–24206 (2019).

10. H. Wang, Z. Lu, Y. Liu, J. Tan, L. Ma, and S. Lin, "Double-layer interlaced nested multi-ring array metallic mesh for high-performance transparent electromagnetic interference shielding," Opt. Lett. **42**(8), 1620–1623 (2017).

11. T. Gao, Z. Li, P.-S. Huang, G. J. Shenoy, D. Parobek, S. Tan, J.-K. Lee, H. Liu, and P. W. Leu, "Hierarchical graphene/metal grid structures for stable, flexible transparent conductors," ACS Nano **9**(5), 5440–5446 (2015).

12. V. V. Tran, D. D. Nguyen, A. T. Nguyen, M. Hofmann, Y.-P. Hsieh, H.-C. Kan, and C.-C. Hsu, "Electromagnetic interference shielding by transparent graphene/nickel mesh films," ACS Appl. Nano Mater. **3**(8), 7474–7481 (2020).

13. L. Ma, Z. Lu, J. Tan, J. Liu, X. Ding, N. Black, T. Li, J. Gallop, and L. Hao, "Transparent conducting graphene hybrid films to improve electromagnetic interference (emi) shielding performance of graphene," ACS Appl. Mater. Interfaces **9**(39), 34221–34229 (2017).

14. R. A. Maniyara, V. K. Mkhitaryan, T. L. Chen, D. S. Ghosh, and V. Pruneri, "An antireflection transparent conductor with ultralow optical loss (<2 %) and electrical resistance (<6 Ωsq^{-1})," Nat. Commun. **7**(1), 13771 (2016).

15. W. Wang, M. Song, T.-S. Bae, Y. H. Park, Y.-C. Kang, S.-G. Lee, S.-Y. Kim, D. H. Kim, S. Lee, G. Min, G.-H. Lee, J.-W. Kang, and J. Yun, "Transparent ultrathin oxygen-doped silver electrodes for flexible organic solar cells," Adv. Funct. Mater. **24**, 1551–1561 (2014).

16. H. Wang, C. Ji, C. Zhang, Y. Zhang, Z. Zhang, Z. Lu, J. Tan, and L. J. Guo, "Highly transparent and broadband electromagnetic interference shielding based on ultrathin doped ag and conducting oxides hybrid film structures," ACS Appl. Mater. Interfaces **11**(12), 11782–11791 (2019).

17. C. Yuan, J. Huang, Y. Dong, X. Huang, Y. Lu, J. Li, T. Tian, W. Liu, and W. Song, "Record-high transparent electromagnetic interference shielding achieved by simultaneous microwave fabry–pérot interference and optical antireflection," ACS Appl. Mater. Interfaces **12**(23), 26659–26669 (2020).

18. D. T. Phan and C. W. Jung, "Multilayered salt water with high optical transparency for EMI shielding applications," Sci. Rep. **10**(1), 21549 (2020).

19. S. Haghanifar, M. McCourt, B. Cheng, J. Wuenschell, P. Ohodnicki, and P. W. Leu, "Discovering high-performance broadband and broad angle antireflection surfaces by machine learning," Optica **7**(7), 784–789 (2020).

20. S. Haghanifar, M. McCourt, B. Cheng, J. Wuenschell, P. Ohodnicki, and P. W. Leu, "Creating glasswing butterfly-inspired durable antifogging superomniphobic supertransmissive, superclear nanostructured glass through Bayesian learning and optimization," Mater. Horiz. **6**(8), 1 (2019).

21. S. Haghanifar, L. M. Tomasovic, A. J. Galante, D. Pekker, and P. W. Leu, "Stain-resistant, superomniphobic flexible optical plastics based on nano-enoki mushroom-like structures," J. Mater. Chem. A **7**(26), 15698–15706 (2019).

22. S. Haghanifar, P. Lu, M. Imrul Kayes, S. Tan, K.-J. Kim, T. Gao, P. Ohodnicki, and P. W. Leu, "Self-cleaning, high transmission, near unity haze OTS/silica nanostructured glass," J. Mater. Chem. C **6**(34), 9191–9199 (2018).

23. S. Haghanifar, R. T. R. D. Vecchis, K.-J. Kim, J. Wuenschell, S. P. Sharma, Ping Lu, P. Ohodnicki, and P. W. Leu, "Flexible nanograss with highest combination of transparency and haze for optoelectronic plastic substrates," Nanotechnology **29**(42), 42LT01 (2018).

24. B. Liang, M. Bai, H. Ma, N. Ou, and J. Miao, "Wideband analysis of periodic structures at oblique incidence by material independent fdtd algorithm," IEEE Trans. Antennas Propagat. **62**(1), 354–360 (2014).

25. D. R. Lide, *CRC Handbook of Chemistry and Physics* (CRC Press, 2007), 88th ed.

26. S. Sarkar, V. Gupta, M. Kumar, J. Schubert, P. T. Probst, J. Joseph, and T. A. König, "Hybridized guided-mode resonances via colloidal plasmonic self-assembled grating," ACS Appl. Mater. Interfaces **11**(14), 13752–13760 (2019).

27. G. E. Fasshauer and M. J. McCourt, *Kernel-based Approximation Methods Using Matlab* (World Scientific, 2015).

28. J. Rapin and O. Teytaud, "Nevergrad - A gradient-free optimization platform," https://GitHub.com/FacebookResearch/Nevergrad (2018).

29. G. Malkomes, B. Cheng, E. H. Lee, and M. Mccourt, "Beyond the pareto efficient frontier: Constraint active search for multiobjective experimental design," in *International Conference on Machine Learning*, (PMLR, 2021), pp. 7423–7434.

30. K. X. Wang, J. R. Piper, and S. Fan, "Optical impedance transformer for transparent conducting electrodes," Nano Lett. **14**(5), 2755–2758 (2014).

31. B. Wang, E. Stevens, and P. W. Leu, "Strong broadband absorption in GaAs nanocone and nanowire arrays for solar cells," Opt. Express **22**(S2), A386–A395 (2014).

32. T. Gao and P. W. Leu, "The role of propagating modes in silver nanowire arrays for transparent electrodes," Opt. Express **21**(S3), A419 (2013).

33. S.-H. Cho and W.-J. Lee, "Effect of added metallic elements in ag alloys on the durability against heat and humidity of indium zinc oxide/ag alloy/indium zinc oxide transparent conductive multilayer system," Jpn. J. Appl. Phys. **49**(11), 111102 (2010).

34. H. Zhou, J. Xie, M. Mai, J. Wang, X. Shen, S. Wang, L. Zhang, K. Kisslinger, H.-Q. Wang, J. Zhang, Y. Li, J. Deng, S. Ke, and X. Zeng, "High-quality azo/au/azo sandwich film with ultralow optical loss and resistivity for transparent flexible electrodes," ACS Appl. Mater. Interfaces **10**(18), 16160–16168 (2018).

35. N. Zhang, Z. Wang, R. Song, Q. Wang, H. Chen, B. Zhang, H. Lv, Z. Wu, and D. He, "Flexible and transparent graphene/silver-nanowires composite film for high electromagnetic interference shielding effectiveness," Sci. Bull. **64**(8), 540–546 (2019).

36. Z. Lu, L. Ma, J. Tan, H. Wang, and X. Ding, "Graphene, microscale metallic mesh, and transparent dielectric hybrid structure for excellent transparent electromagnetic interference shielding and absorbing," 2D Mater. **4**(2), 025021 (2017).

37. A. S. Voronin, Y. V. Fadeev, I. V. Govorun, I. V. Podshivalov, M. M. Simunin, I. A. Tambasov, D. V. Karpova, T. E. Smolyarova, A. V. Lukyanenko, A. A. Karacharov, I. V. Nemtsev, and S. V. Khartov, "Cu–ag and ni–ag meshes based on cracked template as efficient transparent electromagnetic shielding coating with excellent mechanical performance," J. Mater. Sci. **56**(26), 14741–14762 (2021).

38. Y. Han, H. Zhong, N. Liu, Y. Liu, J. Lin, and P. Jin, "In situ surface oxidized copper mesh electrodes for high-performance transparent electrical heating and electromagnetic interference shielding," Adv. Electron. Mater. **4**, 1800156 (2018).